

R. H. Keldermann, M. P. Nash, H. Gelderblom, V. Y. Wang and A. V. Panfilov
Am J Physiol Heart Circ Physiol 299:134-143, 2010. First published Apr 16, 2010;
doi:10.1152/ajpheart.00862.2009

You might find this additional information useful...

This article cites 66 articles, 32 of which you can access free at:

<http://ajpheart.physiology.org/cgi/content/full/299/1/H134#BIBL>

Updated information and services including high-resolution figures, can be found at:

<http://ajpheart.physiology.org/cgi/content/full/299/1/H134>

Additional material and information about *AJP - Heart and Circulatory Physiology* can be found at:

<http://www.the-aps.org/publications/ajpheart>

This information is current as of November 30, 2010 .

Electromechanical wavebreak in a model of the human left ventricle

R. H. Keldermann,^{1*} M. P. Nash,^{2*} H. Gelderblom,³ V. Y. Wang,² and A. V. Panfilov¹

¹Department of Theoretical Biology, Utrecht University, Utrecht, The Netherlands; ²Bioengineering Institute and Department of Engineering Science, The University of Auckland, Auckland, New Zealand; and ³Department of Biomedical Engineering, Eindhoven University of Technology, Eindhoven, The Netherlands

Submitted 10 September 2009; accepted in final form 7 April 2010

Keldermann RH, Nash MP, Gelderblom H, Wang VY, Panfilov AV. Electromechanical wavebreak in a model of the human left ventricle. *Am J Physiol Heart Circ Physiol* 299: H134–H143, 2010. First published April 16, 2010; doi:10.1152/ajpheart.00862.2009.—In the present report, we introduce an integrative three-dimensional electromechanical model of the left ventricle of the human heart. Electrical activity is represented by the ionic TP06 model for human cardiac cells, and mechanical activity is represented by the Niederer-Hunter-Smith active contractile tension model and the exponential Guccione passive elasticity model. These models were embedded into an anatomic model of the left ventricle that contains a detailed description of cardiac geometry and the fiber orientation field. We demonstrated that fiber shortening and wall thickening during normal excitation were qualitatively similar to experimental recordings. We used this model to study the effect of mechano-electrical feedback via stretch-activated channels on the stability of reentrant wave excitation. We found that mechano-electrical feedback can induce the deterioration of an otherwise stable spiral wave into turbulent wave patterns similar to that of ventricular fibrillation. We identified the mechanisms of this transition and studied the three-dimensional organization of this mechanically induced ventricular fibrillation.

ventricular fibrillation; computer simulations; mechanics; electrophysiology; mechano-electrical feedback; stretch-activated channels

MECHANICAL ACTIVITY of the heart is initiated by electrical waves of excitation that propagate through the heart and initiate cardiac contraction. Abnormal excitation of the heart may result in cardiac arrhythmias and the loss of mechanical pump function, leading to sudden cardiac death. Sudden cardiac death caused by cardiac arrhythmias is the most common cause of death in the industrialized world, and, in most cases, this is due to ventricular fibrillation (VF) (73). It has been shown in clinical and experimental studies (11, 17, 26, 41, 46, 62, 68, 70) that VF occurs as a result of the onset of turbulent electrical activation patterns of the heart that are underpinned by multiple reentrant sources of excitation. Mechanisms behind the onset of reentrant sources in the heart and processes resulting in breakup of these sources into complex turbulent activation patterns are of great interest, e.g., in the design of therapeutic strategies to prevent or treat cardiac arrhythmias.

One of the important factors that affects electrical excitation of the heart is mechano-electrical feedback. It has been shown that mechanical deformation alters the electrical properties of myocytes via stretch-activated channels (59), which can change the shape of the action potential in response to stretch (34, 37). Mechano-electric feedback has been studied in the clinical community for well over a century (for reviews, see

Refs. 34, 37, 38) and may have both proarrhythmic and antiarrhythmic consequences. However, the mechanisms underlying these phenomena are not well understood. One of the problems in experimental studies of mechano-electrical feedback is that it is difficult to control and record both the electrical and mechanical properties of cardiac tissue and to alter them in a systematic way. Therefore, alternative methods, such as mathematical modeling, must be used to address this field.

We (47) recently investigated the effects of mechano-electrical feedback on wave propagation using a two-dimensional (2-D) explicitly coupled electromechanical model. We found that it is possible to induce automatic pacemaker activity (52) and spiral wave breakup (53). Both mechanisms are regulated by mechano-electrical feedback via stretch-activated channels. However, in these studies, we chose to use a simple phenomenological model of cardiac excitation in a 2-D isotropic medium. Active tension was generated using an oversimplified isotropic active tension transient. Furthermore, we used an isotropic Mooney-Rivlin material response to describe the passive mechanical properties of the medium.

In the present study, we extended our analyses to an anatomically and functionally realistic electromechanical model of the human left ventricle (LV). We used this approach to study the interactive effects of wave dynamics on mechanical deformation as well as the effect of mechano-electrical feedback on wave dynamics. To this end, in the present report, we introduce a new realistic three-dimensional (3-D) anisotropic electromechanical model of the human LV that combines electrical waves of excitation and mechanical deformation. We validated our model by simulating a control heart beat and compared the deformations with those found experimentally by Ashikaga et al. (2). We used our model to study electrophysiological and mechanical dynamics during reentry in the presence of cardiac contraction. We found that turbulent patterns of excitation during ventricular tachycardia (VT) and VF resulted in desynchronized cardiac contraction compared with a control heart beat. Furthermore, we found that dynamic regions of stretch can cause an otherwise stationary reentrant wave to break up into smaller waves via mechano-electrical feedback of stretch-activated channels.

METHODS

In the present report, we introduce a coupled 3-D electromechanical model of the human LV that combines electrical waves of excitation and mechanical deformation. In this model, electrical excitation waves are described using a detailed ionic cell model of the human ventricular myocyte (64). Mechanical deformations are represented using finite elasticity theory combined with finite element analysis. Based on the local intracellular Ca^{2+} concentration, contractile forces are represented using equations governing the development of tension due to cellular cross-bridge cycling (48). This active tension

* R. H. Keldermann and M. P. Nash contributed equally to this work.

Address for reprint requests and other correspondence: A. V. Panfilov, Dept. of Theoretical Biology, Utrecht Univ., Padualaan 8, Utrecht 3584 CH, The Netherlands (e-mail: A.Panfilov@uu.nl).

is coupled to nonlinear stress equilibrium equations, which are solved using the finite element method. In turn, the resulting mechanical deformations have a feedback effect on the excitation properties of the membrane via tissue deformation and stretch-activated channels. The electrical and mechanical components each have their own numerical discretization. For the electrophysiological model, we created a detailed anatomic finite difference geometry of the LV that contains fiber direction anisotropy. For the mechanical model, we created an equivalent tricubic Hermite finite element geometry that contains the same fiber direction anisotropy. Numerically, the coupled electromechanical model combines a finite difference method approach to integrate the excitation equations, with a Galerkin finite element method to solve the nonlinear equations governing the tissue mechanics. More details are contained in the following sections.

Cardiac Excitation

Excitable behavior was modeled using a monodomain description of cardiac tissue. For this, we used the following partial differential equation (32):

$$C_m \frac{\partial V_m}{\partial t} = \frac{\partial}{\partial x_i} \left(\mathbf{D}_{ij} \frac{\partial V_m}{\partial x_j} \right) - I_{\text{ion}} \quad (1)$$

where C_m is the membrane capacitance, V_m is the transmembrane voltage, t is time, x_i and x_j are spatial coordinates, \mathbf{D}_{ij} is the diffusion tensor accounting for the anisotropy of cardiac tissue (note the implied summation over the spatial coordinates i and j), and I_{ion} is the sum of the ionic transmembrane currents describing the excitable behavior of individual ventricular myocytes. To represent human ventricular electrophysiological properties, we used the ionic TP06 model developed in Ref. 64. This model provides a detailed description of voltage, ionic currents, and intracellular ion concentrations and is based on a wide range of human electrophysiological data. The model reproduces experimentally measured action potential duration (42, 44) and conduction velocity restitution curves (16).

Diffusion tensor \mathbf{D}_{ij} is derived from the fiber direction field. Assuming that the transverse conductivity is the same in all directions orthogonal to the direction of the muscle fiber axis, we described the ventricular conductivity tensor using the following equation:

$$\mathbf{D}_{ij} = D_T \times \delta_{ij} + (D_L - D_T) \alpha_i \alpha_j \quad (2)$$

where D_L and D_T are the longitudinal and transverse diffusion coefficients, respectively, δ_{ij} is the unitary tensor, and α is the muscle fiber vector (with components α_i and α_j). We used 162 $\Omega\cdot\text{cm}$ for D_L and 40.5 $\Omega\cdot\text{cm}$ for D_T , which resulted in conduction velocities of 68 cm/s in the longitudinal direction and 32 cm/s in the transverse direction, similar to the values reported in Ref. 61. The resulting anisotropy ratio was $\sim 2:1$, which was also consistent with clinical measurements (31).

Cardiac Mechanics

To model deformation of the cardiac tissue, the mechanical analysis was based on finite deformation elasticity theory. The normal sarcomere length (SL) of cardiac muscle cells is 2.0 μm (27, 56). In mammals, SLs operate in vivo normally between 1.7 and 2.15 μm (58) and in vitro maximally between 1.5 and 2.3 μm (4, 21, 65, 66). Thus, cardiac cells change their length by 15–20% during contraction (40), and their maximal stretch relative to resting length is ~ 5 –10%.

Following standard continuum mechanics, we used two types of coordinates to refer to a material point in the tissue. Here, $\mathbf{x} = \{x_i\}$ describes the present (deformed) spatial position in rectangular Cartesian coordinates of a material particle that occupied the location $\mathbf{X} = \{X_M\}$ in the reference (undeformed) configuration. The deformation gradient tensor (\mathbf{F}) transforms the undeformed line segment ($d\mathbf{X}$) into the deformed line segment ($d\mathbf{x}$) by $d\mathbf{x} = \mathbf{F} \times d\mathbf{X}$ with $F\{M\} = \partial x_i / \partial X_M$. The right Cauchy-Green deformation (metric) tensor, $\mathbf{C} =$

$\mathbf{F}^T \mathbf{F}$, describes how each component of the undeformed line segment $d\mathbf{X}$ contributes to the squared length of the deformed line segment $d\mathbf{x}$ and is independent of rigid body motion. The Green Lagrange strain tensor (\mathbf{E}) is defined as follows: $\mathbf{E} = 1/2(\mathbf{C} - \mathbf{I})$, where \mathbf{I} is the unitary tensor.

Stress equilibrium. Due to active tension in the cardiac wall and the pressure load on the endocardial surface, the LV model will deform until a new equilibrium state is reached. To determine the deformed state, the stress equilibrium equations are solved using a finite element method. These equations arise from the conservation of linear momentum following Newton's law of motion. In the absence of body forces, the static equilibrium equations reduce to the following:

$$\frac{\partial}{\partial X_M} \left(T^{MN} \frac{\partial x_j}{\partial X_N} \right) = 0 \quad (3)$$

where T^{MN} denotes the components of the second Piola-Kirchhoff stress tensor (note the implied summation over the material coordinates M and N), which represents the force per unit of undeformed area acting on an infinitesimal element of surface in the reference configuration (39). In this study, active and passive stress components were linearly superimposed to define the total state of stress in the tissue (28).

$$T^{MN} = \frac{1}{2} \left(\frac{\partial W}{\partial E_{MN}} + \frac{\partial W}{\partial E_{NM}} \right) - p C^{MN} + T_a \frac{\partial X_M}{\partial x_1} \frac{\partial X_N}{\partial x_1} \quad (4)$$

where W is a strain energy density function described in the next section, E is the Green-Lagrange strain tensor defined above, p is the hydrostatic pressure component based on a Lagrange multiplier approach to maintain incompressibility (45), C^{MN} denotes the components of the contravariant metric tensor (for undeformed orthogonal material coordinates $C^{MN} = \{C_{MN}\}^{-1}$), and T_a is active contractile stress, which is generated only along the myocyte axis. To include length- and velocity-dependent stability, Eq. 4 was further adapted (see Ref. 49).

We assumed that the passive myocardium can be modeled as an incompressible hyperelastic material, described by a transversely isotropic mechanical response (18), as follows:

$$W = \frac{C_1}{2} e^Q \quad \text{and} \quad (5)$$

$$Q = C_2 E_{\text{ff}}^2 + C_3 (E_{\text{tt}}^2 + E_{\text{rr}}^2 + 2E_{\text{tr}}^2) + 2C_4 (E_{\text{ft}}^2 + E_{\text{fr}}^2)$$

where the subscripts f, t, and r describe strains in the fiber, transverse (within the wall plane perpendicular to the fiber direction), and radial (perpendicular to the wall-plane) directions, respectively (see Fig. 1).

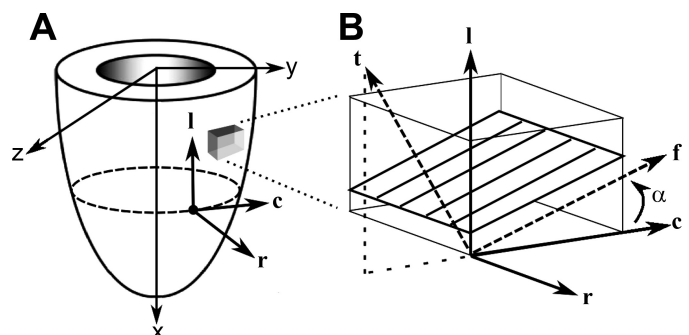


Fig. 1. Schematic representation of the left ventricle (LV) and the cardiac coordinate system (A) and fiber coordinate system (B). See the text for an explanation. α represents the elevation angle (counterclockwise positive) above the short-axis plane between the circumferential and fiber directions (i.e., the fiber angle). In A, c, r, and l are the circumferential, radial, and longitudinal directions; in B, t, f, and r are the transverse, fiber, and radial directions.

We used material parameters based on Ref. 51: $C_1 = 1.2$ kPa, $C_2 = 26.7$, $C_3 = 13.5$, and $C_4 = 14.7$. The material properties were assumed to be homogeneous throughout the LV wall.

To represent active contractile tension T_a , we used the Niederer-Hunter-Smith (NHS) model (48). The NHS contraction model uses three input variables: the intracellular Ca^{2+} concentration, the fiber extension ratio, and the velocity of fiber shortening. The intracellular Ca^{2+} concentration is generated by the TP06 model (Eq. 1), whereas the other two parameters are obtained from the 3-D mechanics model. The NHS model is based on experimental data from rat and guinea pig hearts at room temperature and was designed to operate under physiological SLs in the range $1.8 < \text{SL} < 2.3$ μm . We adjusted the parameters of the NHS model to account for the longer action potential and different Ca^{2+} transients of the TP06 model. On the advice of Dr. Niederer, we first sped up the relaxation kinetics of the NHS model by setting $\alpha_{r1} = 10 \text{ s}^{-1}$ and $\alpha_{r2} = 25 \text{ s}^{-1}$, which is consistent with the faster cardiac relaxation times reported for higher body temperatures (12, 55). We also set the parameters for contractile tension to $T_{\text{ref}} = 125$ kPa and $\text{pCa}_{50} = 6.5$, which is again consistent with the temperature increase (20). Such modifications were necessary because when the original parameter values were used, the longer action potential duration and Ca^{2+} dynamics in human ventricular myocytes (represented by the TP06 model) resulted in the accumulation of contractile tension during higher stimulation frequencies in the NHS model, even though intracellular Ca^{2+} was restored to resting values between stimuli. With these new model parameters, the NHS model generated maximal contractile tension values of ~ 100 kPa at resting SL. For further model information and parameters, see Ref. 48.

Mechanoelectrical Feedback

Tissue deformation. The equations describing electrical activity (Eq. 1) can be rewritten by taking local coordinate deformation into account:

$$C_m \frac{\partial V_m}{\partial t} = \frac{1}{\sqrt{C}} \frac{\partial}{\partial X_M} \left(\sqrt{C} D_{MN} C^{NL} \frac{\partial V_m}{\partial X_L} \right) - I_{\text{ion}} \quad (6)$$

where D_{MN} denotes the components of the diffusion tensor (note the implied summation over the material coordinates M , N , and L), C^{NL} denotes the components of the contravariant metric tensor, and $C = \det(C_{NL})$ and is the determinant of the covariant metric tensor [$\det(C_{NL}) = 1$ for an incompressible medium].

Stretch-activated channels. The direct influence of deformation on the excitation properties is via stretch-activated current (I_s), which was added to the TP06 model. There are three main groups of mechanically activated channels in the heart, but only two of them (cation nonselective channels and K^+ -selective channels) are activated by stretch (37). The overall physiological action of these channels is depolarization of the membrane in response to stretch, as shown in the majority of experimental observations from isolated cardiac tissue. Experimental studies (25, 72, 74) of the electrophysiological properties of stretch-activated channels have shown that they are instantly activated by mechanical stimulation and that the current-voltage relationship for the most important nonspecific cation channels is linear. On basis of these observations, linear ionic models for I_s have been proposed (67, 69). These linear models have been used to study the effects of mechanical stretch on heart tissue using detailed ionic models of cardiac myocytes. We followed this approach and used the following nonselective linear time-independent description of I_s :

$$I_s = G_s \frac{(\lambda_f - 1)}{(\lambda_{\text{max}} - 1)} (V_m - E_s) \quad (7)$$

where G_s and E_s are the maximal conductance and reversal potential of stretch-activated channels, respectively, and $\lambda_f = C_{\text{ff}} = 2E_{\text{ff}} + 1$ and is the myocyte axis extension ratio, which is normalized by the

maximal extension (λ_{max}). We assumed that cells can maximally stretch by 10% and thus set $\lambda_{\text{max}} = 1.1$. Following Ref. 52, I_s in Eq. 7 is only present if $E_{\text{ff}} > 0$ (which indicates stretch in fiber direction); otherwise, I_s is zero.

The value of E_s in most biophysical models is assumed to be around -20 mV (25, 67, 69) and describes the experimentally observed depolarizing effect of I_s . The value of G_s varies up to 100 $\mu\text{S}/\mu\text{F}$ (36, 37, 67). We used G_s values between 0 and 75 $\mu\text{S}/\mu\text{F}$ to investigate the effects of I_s on the excitation properties.

Human LV Anatomy

The geometric data describing the 3-D ventricular anatomy and fiber direction field were derived from a structurally normal human heart (23, 24) and are described in more detail in Ref. 63. This dataset had an isotropic resolution of 0.5 mm. The muscle fiber direction field was constructed based on general knowledge of the fiber architecture in the human heart (60) combined with detailed data on the fiber architecture of the canine heart (50). We removed points corresponding to the right ventricle for the human dataset. The remaining 1,118,053 voxels were used as a finite difference mesh for the electrical part of our framework.

For the mechanical equations, we developed a finite element mesh based on the finite difference data. We extracted the endocardial and epicardial surfaces from the LV dataset. To fit a finite element mesh to these data, we created an initial mesh in the shape of a truncated ellipsoid using tricubic Hermite hexahedral elements. The mesh consisted of one element in the radial direction, five elements in the longitudinal direction, and eight elements in the circumferential direction (40 tricubic Hermite elements containing 2,386 geometrical degrees of freedom). The model was then fitted using a nonlinear geometric face-fitting procedure (8). The endocardial and epicardial surfaces of the mesh were fitted to 34,177 and 103,319 data points, respectively. For this, we used an iterative method in which the Euclidean distance between all data points and their orthogonal projections to the model mesh were minimized.

The 3-D model fiber angles were fitted using a similar nonlinear optimization method. The fiber angle field contained 656 degrees of freedom, which were fitted to 10,904 fiber angles. Through the LV wall, fiber angles varied from 13 (endocardium) to -55° (epicardium) in the anterior region, 72 to -32° in the posterior wall, 62 to -57° in the lateral free wall, and 14 to -37.3° in the septum (elevation angles are defined with respect to the local short-axis plane). These fiber orientations were similar to measurements of fiber orientations reported in Ref. 60. The resulting root mean square error after fitting was 10° , similar to that reported in Ref. 15. For more information on how to create a mathematical model of geometry and fibrous structure of the heart, we refer to Refs. 8 and 50.

Numerical Methods

The coupled electromechanical model was solved using a hybrid approach that incorporates a finite difference method to solve the electrical equations and finite element techniques to compute the deformation of the tissue. The electromechanical simulations are typically performed on two distinct time scales: one for the electrophysiology and a longer time scale for the mechanics.

For electrical excitation, we used a finite difference method with an adaptive time step of up to $\Delta t = 0.02$ ms on a grid containing 1,118,053 points with a space step of $\Delta x = 0.5$ mm. The Laplacian in Eq. 6 was computed using weights calculated at each point based on the local conductivity and metric tensor. To impose no-flux boundary conditions, the current flow through the surface of the heart to nonheart points was set to zero by adjusting the weights of the boundary points (63).

Mechanical equations (Eq. 3) were solved using CMISS (www.cmiss.org), which was developed at the University of Auckland. Each mechanical step was followed by 100 electrical steps. Excitation-

contraction coupling was achieved by passing spatial distributions of contractile tension from the electrophysiology model to the mechanical component of our framework. The mechanical boundary conditions included fixation of the upper basal ring and application of a constant endocardial cavity pressure load of 10 kPa. After the solution of each mechanical deformation, metric tensors were updated and passed back to the electrophysiology model at 41,380 points, which were further interpolated to all electrical elements. These metric tensors were then used to compute the new weights for evaluation of the Laplacian in Eq. 6 and to calculate the current generated via stretch-activated channels (Eq. 7).

To simulate cardiac excitation during normal sinus rhythm, we stimulated the entire endocardium with a period of 600 ms. To initiate 3-D scroll waves, we used an S1-S2 protocol, for which an S1 stimulus was applied in the septum. The S2 stimulus was activated during the refractory tail of the S1 stimulus on the posterior LV wall and was extended from the base to ~50% of the base-apex dimension, thereby creating a single reentrant scroll wave on the posterior LV. All stimuli were applied at twice the diastolic threshold for a duration of 10 ms.

Pseudo-body surface ECGs were computed using the infinite volume conductor approach (57) as follows:

$$\text{ECG} = \int_V \frac{D \nabla V_m \cdot \vec{r}}{r^3} dV \quad (8)$$

where V is the domain of integration (i.e., the ventricular volume), \vec{r} is the vector from each point to the recording electrode, which was placed 10 cm from the center of the LV in the anterior direction of the transverse plane, and r is the radius. Methods for the detection of scroll wave filaments are described in Ref. 63.

Simulations were run on a Dell Precision Workstation (dual Intel Xeon 2.8 GHz, 2 GB RAM). Simulating 1 s of wave propagation and deformation of the LV took ~18 h of wall clock computation time, which was split approximately equally between the electrical and mechanical components of our model. Ventricular geometry, wave patterns, and scroll wave filaments were visualized using the marching cubes algorithm for isosurface detection in voxel data and OpenGL for isosurface rendering. Mechanical deformation was visualized using cmgui (www.cmiss.org/cmgui).

RESULTS

Model Validation

We compared our results with the experimental deformations reported by Ashikaga et al. (2) (Fig. 3, atrial pacing). In five canine hearts, they recorded strains referred to local cardiac coordinates in the anterior wall of the LV (between the first and second diagonal branches of the left anterior descending coronary artery) during normal atrioventricular conduction. We only compare end-systolic strains, because Ashikaga et al. (2) refer strains to the end-diastolic state.

We computed strains with respect to cardiac and fiber coordinates under control conditions and compared these with experimental values (2). With reference to Fig. 1A, cardiac coordinate were defined by the orthogonal system (c , l , and r), where c is the short-axis circumferential direction tangent to the wall plane, l is the longitudinal axis tangent to the ventricular surface from the apex to base, and r is the transmural axis directed from the endocardium to epicardium. We also defined fiber coordinates using the orthogonal system (f , t , and r), where f is the myocyte (fiber) axis, t lies transverse to the fiber axis within the ventricular wall plane, and r is the radial coordinate, as defined above (Fig. 1B).

Figure 2 shows the epi-, mid-, and endocardial cardiac strains at three different transmural points approximately halfway between the base and apex within the anterior LV wall. We showed cardiac normal strains [circumferential (E_{cc}), longitudinal (E_{ll}), and radial (E_{rr})] and cardiac shear strains [circumferential-longitudinal (E_{cl}), longitudinal-radial (E_{lr}), and circumferential-radial (E_{cr})]. Note that for comparison with the experimental recordings from Ashikaga et al. (2), we calculated these cardiac strains with respect to the end-diastolic configuration with a LV pressure of 1 kPa. It should be noted that no tuning of the mechanical constitutive parameters was performed as part of this study.

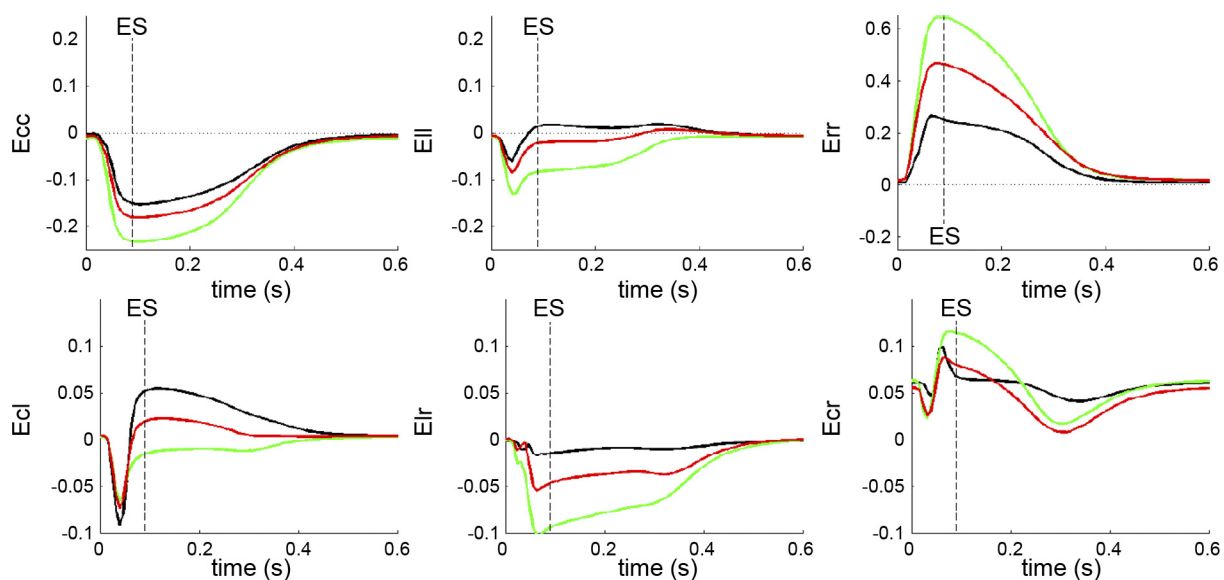


Fig. 2. Cardiac normal strains (E_{cc} , E_{ll} , and E_{rr}) and shear strains (E_{cl} , E_{lr} , and E_{cr}) for the anterior LV wall under control conditions, showing the subepicardial (black), midwall (red), and subendocardial (green) strain transients. ES, end systole (dashed line). Note that for comparison with the experimental recordings from Ashikaga et al. (2), all strains shown here have been referred to the end-diastolic configuration. For explanation of strain components, see the text.

We found that the normal strains E_{cc} , E_{ll} , and E_{rr} (denoted as E_{11} , E_{22} , and E_{33} , respectively, in Ref. 2) were generally in good agreement, although our model slightly overestimated end-systolic wall thickening. The transmural gradients in the cardiac normal strains also compared well with the experimental data. The epicardial in-plane shear strain E_{cl} (E_{12}) matched well; however, endocardial E_{cl} was small. The magnitude and transmural gradient of the longitudinal transverse shear E_{lr} (E_{23}) were consistent; however, E_{lr} was of the opposite sign to the recordings. This may be explained by the lack of orthotropic sheet structure in our model, which has been shown to affect transmural shear (10). The short-axis transverse shear E_{cr} (E_{13}) was also in good agreement. All transmural gradients in the cardiac shear strains were consistent with the experimental recordings.

We also computed several electrical and mechanical characteristics of the model during normal cardiac excitation. Figure 3 shows the pseudo-ECG, which resembles a normal ECG during sinus rhythm. The QRS complex corresponds to the depolarization of the ventricle and lasted ~ 90 ms. The T wave represents the repolarization (or recovery) of the ventricle, and the QT interval was ~ 360 ms, which was similar to clinically recorded ECGs during control heart cycles (19). Figure 3 also shows the volume fraction, which represents the deformed cavity volume as a proportion of the end-diastolic volume. This corresponds with an end-systolic LV ejection fraction of 58%, which is in accordance with that of the healthy heart (19).

For LV endocardial pacing, we found multiple phases of deformation, as exemplified by the fiber extension ratio λ_f (see Fig. 3). We found fiber shortening ($\lambda_f < 1$) during systolic contraction, over which myocytes change their length by up to 12%. After systole, myocyte stretch ($\lambda_f > 1$) occurred due to the LV cavity pressure of 10 kPa applied to the endocardial surface. Myocyte stretch relative to the resting length was between 5% and 10%.

Simulating a Stable Reentrant Spiral

As described in METHODS, we initiated a spiral wave on the posterior wall of the LV. For this simulation, we set up the conductivity of the stretch-activated channels to be zero ($G_s = 0$). The spiral wave remained stable for the entire duration of the simulation. Figure 4 shows the ECG, which was periodic (dominant frequency of 4.0 Hz), resembling ECG signals observed during VT. The dominant frequency corresponds to the period of the spiral wave. Figure 4 also shows the relative

change in the LV cavity volume expressed as a fraction of the end-diastolic volume. The first two oscillations correspond to the initiation of the spiral wave during the S1-S2 protocol. Subsequently, we observed that the average volume of the LV cavity decreased by $\sim 50\%$ and oscillated with an amplitude of 8–10% and a dominant frequency of 4.0 Hz. The slow rise in volume fraction can be explained via intracellular Ca^{2+} ; at higher frequencies, the peak values of intracellular Ca^{2+} slightly decrease, and thus less contractile tension is generated.

In addition, Fig. 4 shows the epi-, mid-, and endocardial fiber extension ratio (λ_f) at the same locations as in the control simulation (Fig. 2). We observed fiber shortening ($\lambda_f < 1$) and local wall thickening (not shown) during reentry. Fiber extension oscillated with the same frequency as that of the spiral wave. We also found that the 3-D distribution of λ_f varied throughout the LV during reentry and that multiple regions of the LV wall were subject to fiber stretch ($\lambda_f > 1$) at various times. These regions of fiber stretch dynamically shifted across the LV myocardium and were dependent on the phase of the spiral wave and location of wavefronts and were often located ahead of the wavefront adjacent to contracted tissue behind the wavefront.

Mechanically Induced Wavebreak

To investigate mechanically induced wavebreak, we incorporated stretch-activated channels with a conductivity of $G_s = 75 \mu S/\mu F$ into the electrophysiology model and induced a spiral wave on the posterior wall of the LV. All other parameters were the same as for the stable spiral wave simulation. After the initiation of the spiral, we observed wavebreaks, which were enhanced over time by the stretch-related processes. From the wavefronts (Fig. 5), we observed that the initial spiral wave on the posterior wall remained stable throughout the simulation. We also observed wavebreaks on both the posterior and anterior walls, but not close to the core of the initial spiral wave.

Figure 6 shows the pseudo-ECG for this simulation. The ECG was more irregular and complex compared with that of the stable spiral simulation. The dominant frequency was 3.6 Hz, similar to frequencies reported in clinical (9, 43, 46, 71) and numerical (63) studies of VF. The slightly lower frequency compared with control can be explained by the activation of I_s , which leads to a localized decrease in Na^+ current, resulting in lower conduction velocities ahead of the wavefront. Figure 6 also shows the time dynamics of the number of filaments found in the LV during 8 s of simulation. Over the first 4 s, the

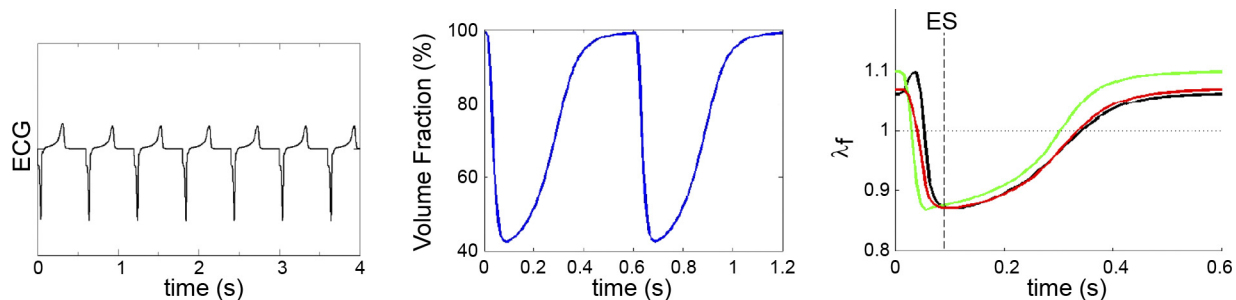


Fig. 3. Electrical and mechanical characteristics under control conditions. *Left*: pseudo-ECG. *Middle*: volume fraction relative to end-diastolic volume. *Right*: fiber extension ratio (λ_f) observed at the anterior wall of the LV, showing subepicardial (black), midwall (red), and subendocardial (green) transients. Note that λ_f is referred to the pre-diastolic resting sarcomere length with a LV cavity pressure of 0 kPa.

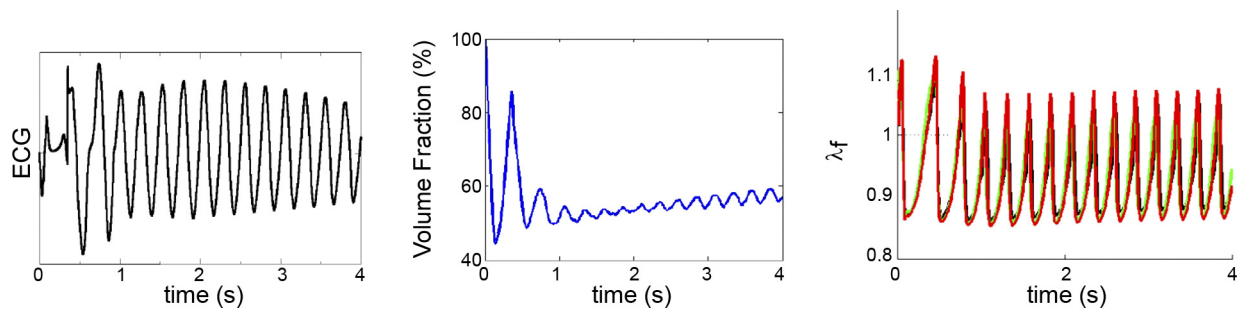


Fig. 4. Electrical and mechanical characteristics during stable spiral simulation. *Left*: pseudo-ECG. *Middle*: volume fraction relative to end-diastolic volume. *Right*: λ_f observed at the anterior wall of the LV, showing subepicardial (black), midwall (red), and subendocardial (green) transients. Note that λ_f is referred to the prediastolic resting length with a LV cavity pressure of 0 kPa.

number of filaments steadily increased from 1 (the initial spiral) to over 15. Between 4 and 8 s of time, the number of filaments slightly decreased and oscillated around 13. The average number of filaments found during the last 4 s was 13.6. In addition, Fig. 6 shows a typical example of the number of filaments present during developed VF. As shown in Figs. 5 and 6, there were clearly multiple independent filaments, while the initial spiral wave remained intact.

After the initial phase and resulting mechanically induced wavebreaks, we found that the LV remained in a contracted state, similar to that of the stable spiral simulation. The LV cavity volume fraction, mechanical 3-D deformations, and fiber strains were similar to those of the stable spiral simulation shown in Fig. 4.

We analyzed how filaments were created and destroyed over time through death, birth, bifurcation, and amalgamation events (see

Fig. 7). The horizontal lines in Fig. 7 indicate individual filaments and their lifespan. The start of a line is determined by the birth of a filament or the bifurcation from another filament. The righthand end of each line indicates when a filament disappears due to the death or the amalgamation of a filament with another filament. In Fig. 7, the short horizontal lines correspond to short-living filaments and long lines correspond to more persistent filaments. During the 8 s of simulation time, we detected 1,276 filaments with 453 births, 496 deaths, 824 bifurcations, and 781 amalgamation events. As shown in Fig. 7, the initial spiral remained intact for the entire 8 s (bottom red line). Most of the filaments existed for a short period of time, although we also observed a small number of persistent independent filaments.

We investigated the effects of different levels of activation of stretch-activated channels (G_s) on the VF dynamics. For

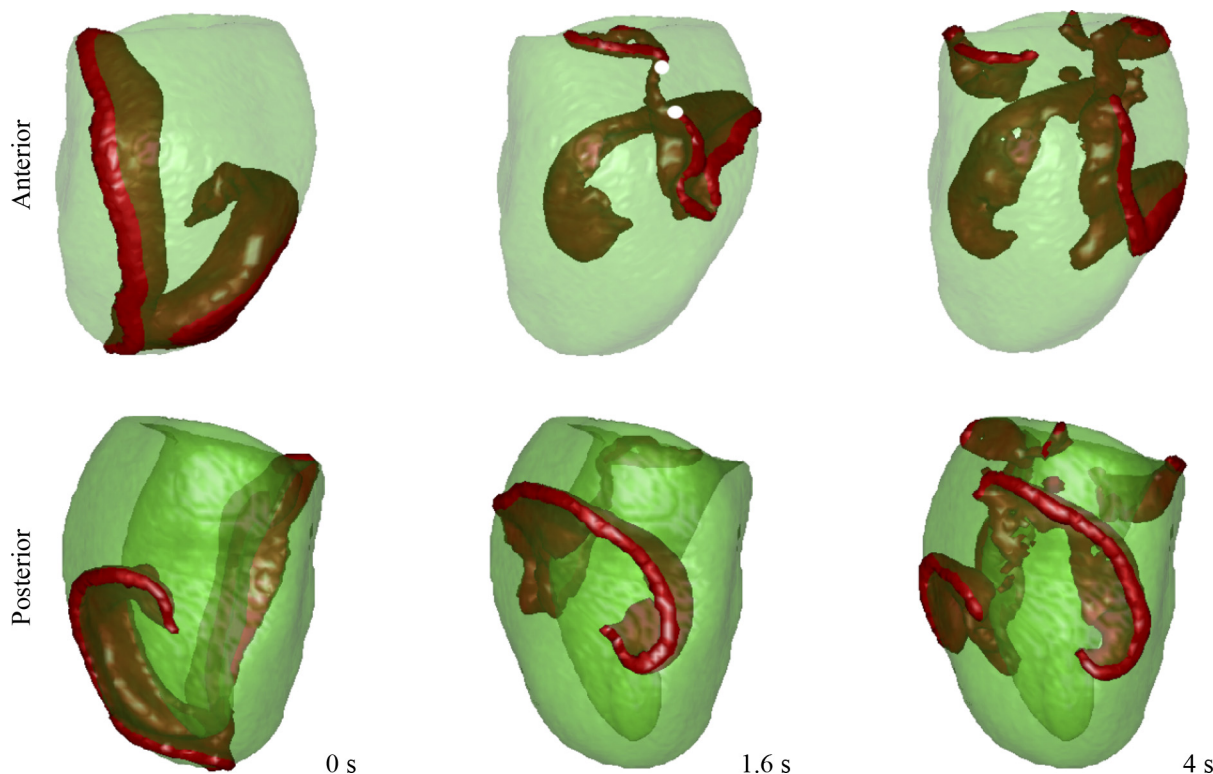


Fig. 5. Wavefronts. *Top*: anterior view. *Bottom*: posterior view. From *left to right*, the first snapshot shows the spiral after its initiation on the posterior side of the LV. The second snapshot shows the first wavebreak found on the anterior side (between the white circles) after ~ 1.6 s of simulation time. The third snapshot shows the wave pattern after ~ 4 s of simulation time. Note that multiple waves are present, while the initial spiral wave remains intact.

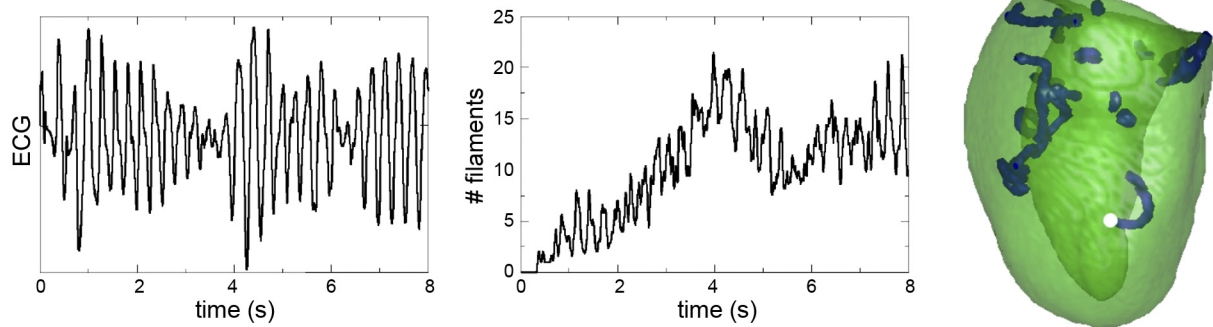


Fig. 6. Mechanically induced breakup. *Left*: pseudo-ECG. *Middle*: number of filaments for maximal conductance (G_s) = 75 $\mu\text{S}/\mu\text{F}$. *Right*: snapshot showing the number of filaments after ~ 4 s of simulation time. The white circle indicates the initial filament spiral.

this, we repeated the above simulations with G_s set to 0, 30, 45, 60, and 75 $\mu\text{S}/\mu\text{F}$ and analyzed the number of filaments present during the simulation (see Fig. 7). For $G_s = 30$ $\mu\text{S}/\mu\text{F}$, we found that the simulation remained stable during 4 s of simulation time, although a small number of wavebreaks were observed toward the end of the simulation. For larger G_s values, we observed that the number of filaments steadily increased over time with more filaments created for larger values of G_s , thereby also increasing the complexity of the VF dynamics.

The filament history dynamics shown in Fig. 7 resemble those of mother rotor fibrillation (33). However, this may just be a visual coincidence, since based on these results alone we cannot claim that the wavebreaks are driven by the initial spiral wave, nor can we claim that these breaks disappear if the initial spiral wave is removed. On the other hand, we can explain such filament dynamics by the maximal stretch distribution observed during the simulation. Figure 8 shows the maximal fiber extension values observed at each epicardial point on both the anterior and posterior free walls during the first 4 s of the simulation. We observed regions of stretch ($\lambda_f > 1$) on the anterior free wall, where most breaks are located. In contrast, we observed that stretch did not occur ($\lambda_f < 1$) close to or around the core of the initial spiral wave on the posterior wall.

The mechanism by which stretch of the tissue induces wavebreak can be explained in the following way. Stretch-activated channels produce an inward current, which depolarizes the myocyte membrane. This depolarization is not suffi-

cient to generate an action potential (i.e., it is subthreshold); however, it leads to a quite opposite effect: a depression of excitability. This occurs as a result of voltage-dependent inactivation of the Na^+ channel. In 1952, Hodgkin and Huxley (22) showed that slow depolarization of a nerve cell membrane results in the progressive inactivation of Na^+ channels. Such inactivation was also found in cardiac cells (see, e.g., Ref. 3) and is present in all ionic models of cardiac cells. Thus, stretch-induced membrane depolarization inactivates Na^+ channels, which carry the main ionic current underlying the initiation of the action potential upstroke. As a consequence, a wave that arrives in a region of substantial stretch cannot propagate through that region, and wavebreak is formed. We (53) have previously presented a detailed study of this process using a low-dimensional model of cardiac tissue. We have also performed simulations using a higher-dimensional model, which combined the mechanics used in Ref. 53 with the biophysical TP06 ionic model of cardiac excitation. *Video 1* in the Supplementary Material shows the results of simulations performed in a simple 2-D geometry on a grid of 705×705 elements with space step of 0.25 mm.¹ We found that in this case, I_s induces the break up of an otherwise stable single spiral wave into a complex spatiotemporal pattern. Since these 2-D simulations were performed using a space step of 0.25 mm, this

¹ Supplemental Material for this article is available online at the *American Journal of Physiology-Heart and Circulatory Physiology* website.

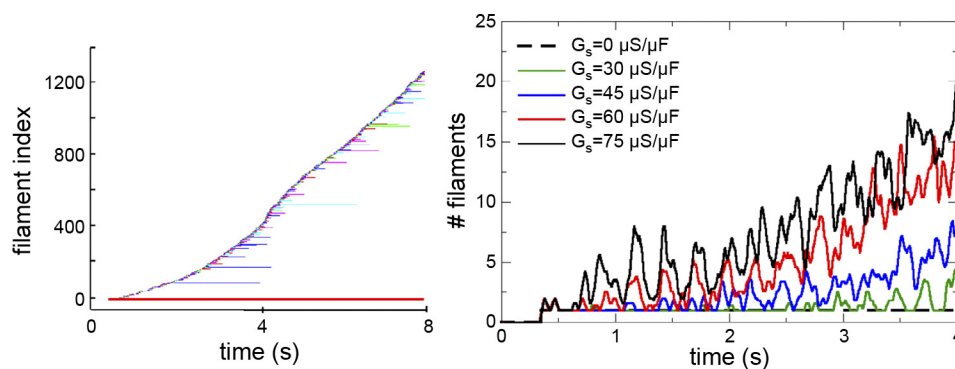


Fig. 7. *Left*: filament history. $G_s = 75$ $\mu\text{S}/\mu\text{F}$. Horizontal lines correspond to individual filaments and start at the time that a filament appears (through birth or bifurcation) and stop at the time that a filament disappears (through death or amalgamation). Colors indicate clusters of filaments that can be traced back through bifurcation events to a unique initial filament. We used different colors for filaments with the same ancestor only if the filament cluster had a size of 5 or more filaments. All other filaments that either arose through birth rather than bifurcation or belong to a small cluster are colored black. The long red line at the bottom represents the initial spiral, which persisted through the entire simulation. *Right*: number of filaments over time for $G_s = 0, 30, 45, 60$, and 75 $\mu\text{S}/\mu\text{F}$.

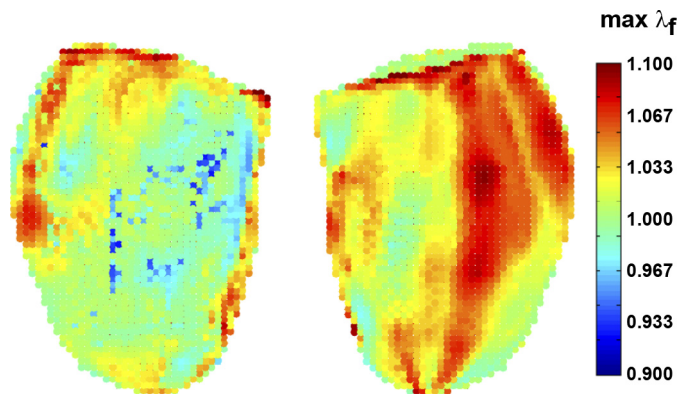


Fig. 8. Maximal λ_f observed at each point during the first 4 s of simulation time. *Left*: posterior view. *Right*: anterior view. The initial spiral was located on the posterior wall in the region where no stretch was observed. Red areas ($\lambda_f > 1$) highlight regions where stretch-activated currents are generated, whereas blue areas ($\lambda_f < 1$) indicate regions where the fibers are in a shortened state.

also indicates that the break up observed in this study is not a result of a coarse spatial discretization. Upon further investigation, we confirmed that the mechanism of this effect is, again, the voltage-dependent inactivation of Na^+ channels.

DISCUSSION

In this study, we developed a 3-D strongly coupled electromechanical model of the human LV to investigate the interactive effects of electrical waves and mechanical contraction during reentry. This 3-D electrophysiological model contains a detailed description of human LV anatomy and fiber direction anisotropy and represents the electrophysiological properties of human ventricular myocytes using the ionic TP06 model (64). This model contains detailed descriptions of voltage, ionic currents, and intracellular ion concentrations and is based on a wide range of human electrophysiological data. The intracellular Ca^{2+} concentration of the TP06 model was used as input for the biophysical NHS model of cardiac tissue contraction (48), which represents the contractile tension developed due to molecular cross-bridge cycling. This active tension is coupled to a 3-D finite element model of passive mechanics, which represents the same human LV anatomy and fiber direction anisotropy as described above for the electrophysiology model. The mechanical model was subjected to a transversely isotropic exponential material response to describe the passive properties. The stress equilibrium equations were solved to calculate the deformed state of the LV and the corresponding local metric tensors. Mechanoelectrical feedback was introduced via local metric tensors by updating the local coordinate system and by calculating the local deformation, which modulates I_s .

We validated our LV electromechanical model using a control excitation, for which we stimulated the entire LV endocardium. We observed $\sim 10\%$ fiber shortening (compared with resting length) and $\sim 15\%$ wall thickening during systolic contraction. End-systolic cardiac strain distributions were similar to experimental recordings reported from canine hearts during normal atrioventricular conduction (2). The end-systolic ejection fraction was 58%, corresponding to that of a healthy human heart.

The mechanisms of wavebreak studied in this report are substantially different from other mechanisms of breakup, such

as negative filament tension (1, 5), fiber rotation (14), and restitution (54). The onset of breakup by our mechanism does not require the presence of any of the above factors. Mechanically induced breakup is strongly associated with the deformation of the heart and the presence of stretch-activated channels and will not occur in the absence of either of these factors.

One obvious experimental validation of the effects of stretch-activated channels on wave breakup might be a study that compares the onset of fibrillation in a normal heart and in a heart in which stretch-activated channels are blocked (e.g., by gadolinium). One study (6) has shown that gadolinium indeed decreases the vulnerability of rabbit hearts to atrial fibrillation; however, to the best of our knowledge, such experimental studies have not yet been performed for ventricles. It should also be noted that the interpretation of the results of such experiments may be not so straightforward since it is well known that, in addition to block of stretch-activated channels, gadolinium has additional important membrane effects (see, e.g., Ref. 75).

Although our data show a new possibility of wavebreak in the heart, we do not claim that all VF episodes occur due to mechanoelectrical feedback. There are, of course, multiple experimental studies showing that VF can be induced during complete block of cardiac contraction caused by the application of excitation-contraction decouplers used in optical mapping studies (see, e.g., Refs. 13 and 17). On the other hand, the mechanisms considered in the present study are more likely to occur in conditions where stretch of the tissue is more substantial or is combined with other pathological factors, such as ischemia or infarction. In fact, the results reviewed by Janse et al. (29) show that the trigger for VF during phase 1B of ischemia is most likely related to stretch [see also a recent modeling study (30)].

During mechanically induced breakup, we did not observe any wavebreaks close to the core of the spiral, resulting in mother rotor-like VF patterns. Especially in the initial phase of the simulation, we found that wavebreaks were small and dependent on the initial spiral wave. The complexity of the simulation increased as time increased, enhancing wavebreaks over time due to the stretch-related processes. The complexity of VF dynamics is dependent on the amount of stretch generated (e.g., determined by λ_f , intracellular Ca^{2+} , T_a , passive material properties, etc.) and the magnitude of I_s (determined by G_s and E_s). We observed that the complexity of VF and number of filaments increased when G_s increased.

These preliminary results demonstrate that mechanoelectric feedback can cause an otherwise stationary spiral wave to break up, thus providing one possible explanation for the degeneration of VT to VF activity. The effects shown here should be considered as an indication of the importance of mechanics on wave dynamics and not as a firmly established mechanism. Further experimental research and numerical studies for variations of initial conditions, boundary constraints, and model parameters are needed to quantify the effects of mechanoelectrical feedback on wave dynamics. In general, mechanoelectrical feedback has multiple effects on the electrical activity of the heart, which are not limited to the factors studied in this report. Extensive reviews and a dedicated editorial on this subject are contained in Ref. 38.

Limitations

We adopted an isotonic loading regime with a constant LV endocardial pressure of 10 kPa. During the normal cardiac cycle, there are variations in LV pressure and volume. This can be improved using a Windkessel afterload model (7, 35). However, such pressure-volume loops are typically not present during VT or VF since cardiac output is often significantly compromised.

Our geometric model only contained fiber orientations. Thus, the LV model did not account for sheet or imbrication angles, which may affect local mechanics, such as transverse shear deformations, or the strains near the apex and base (15). In addition, the effects of the right ventricle on electromechanical dynamics were not accounted for in this study, but this will be addressed in future research.

The mechanical properties of the LV myocardium were described using a transversely isotropic material relation, with parameters based on experimental data from the canine ventricular myocardium. The parameters of the active tension model were based on experimental data from rats. For the present purposes, we made minor adjustments to some parameters to avoid tension accumulation during high-frequency contractions. A similar active contractile mechanics model needs to be developed based on human experimental contraction data to determine the correct parameters and maximum tension values.

Mechano-electrical feedback was modeled via the modulation of diffusion pathways and I_s . Mechanical deformation may also affect the passive electrical properties and other ionic currents of cardiac myocytes. At present, however, limited experimental data are available upon which represent such feedback mechanisms.

While we have identified some important issues above, the conclusions of the present study do not depend on these limitations. Indeed, these additional features and effects may introduce other interesting dynamics and electromechanical interactions.

ACKNOWLEDGMENTS

The authors gratefully acknowledge advice provided by Dr. S. Niederer regarding the parameter adjustment of the NHS contraction model and thank Dr. R. Hren for providing anatomic data for the simulations.

GRANTS

This work was funded by The Netherlands Organization for Scientific Research Grants 814.02.014 and 635.100.004. A. V. Panfilov was partially supported by the Institut des Hautes Etudes Scientifiques (Bures-sur-Yvette, France) and the James Simons Foundation. M. P. Nash is supported by a James Cook Research Fellowship from the Royal Society of New Zealand.

DISCLOSURES

No conflicts of interest, financial or otherwise, are declared by the author(s).

REFERENCES

- Alonso S, Panfilov AV. Negative filament tension in the Luo-Rudy model of cardiac tissue. *Chaos* 17: 015102, 2007.
- Ashikaga H, Omens JH, Ingels NB, Covell JW. Transmural mechanics at left ventricular epicardial pacing site. *Am J Physiol Heart Circ Physiol* 286: H2401–H2407, 2004.
- Berman MF, Camardo JS, Robinson RB, Siegelbaum SA. Single sodium channels from canine ventricular myocytes: voltage dependence and relative rates of activation and inactivation. *J Physiol* 415: 503–531, 1989.
- Bers DM. *Excitation-Contraction Coupling and Cardiac Excitation Force* (3rd ed.). Dordrecht, The Netherlands: Kluwer Academic, 2001.
- Biktashev VN, Holden AV, Zhang H. Tension of organizing filaments of scroll waves. *Philos Trans R Soc Lond A Math Phys Sci* 347: 611–630, 1994.
- Bode F, Katchman A, Woosley RL, Franz MR. Gadolinium decreases stretch-induced vulnerability to atrial fibrillation. *Circulation* 101: 2200–2205, 2000.
- Bovendeerd PH, Arts T, Huyghe JM, Van Campen DH, Reneman RS. Dependence of local left ventricular wall mechanics on myocardial fiber orientation: a model study. *J Biomech* 25: 1129–1140, 1992.
- Bradley CP, Pullan AJ, Hunter PJ. Geometric modeling of the human torso using cubic Hermite elements. *Ann Biomed Eng* 25: 96–111, 1997.
- Clayton RH, Murray A, Campbell RW. Objective features of the surface electrocardiogram during ventricular tachyarrhythmias. *Eur Heart J* 16: 1115–1119, 1995.
- Costa KD, Takayama Y, McCulloch AD, Covell JW. Laminar fiber architecture and three-dimensional systolic mechanics in canine ventricular myocardium. *Am J Physiol Heart Circ Physiol* 276: H595–H607, 1999.
- Davidenko JM, Pertsov AM, Salomonsz R, Baxter W, Jalife J. Stationary and drifting spiral waves of excitation in isolated cardiac muscle. *Nature* 355: 349–351, 1992.
- De Tombe PP, Stienen GJ. Impact of temperatures on cross-bridge cycling kinetics in rat myocardium. *J Physiol* 584: 591–600, 2007.
- Efimov IR, Nikolski VP, Salama G. Optical imaging of the heart. *Circ Res* 95: 21–33, 2004.
- Fenton F, Karma A. Vortex dynamics in three-dimensional continuous myocardium with fiber rotation: filament instability and fibrillation. *Chaos* 8: 20–47, 1998.
- Geerts L, Bovendeerd PH, Nicolay K, Arts T. Characterization of normal cardiac myofiber field in goat measured with MR-diffusion tensor imaging. *Am J Physiol Heart Circ Physiol* 283: H139–H145, 2002.
- Girouard SD, Pastore JM, Laurita KR, Gregory KW, Rosenbaum DS. Optical mapping in a new guinea pig model of ventricular tachycardia reveals mechanisms for multiple wavelengths in a single reentrant circuit. *Circulation* 93: 603–613, 1996.
- Gray RA, Pertsov AM, Jalife J. Spatial and temporal organization during cardiac fibrillation. *Nature* 392: 75–78, 1998.
- Guccione JM, McCulloch AD, Waldman LK. Passive material properties of intact ventricular myocardium determined from a cylindrical model. *J Biomech Eng* 113: 42–55, 1991.
- Guyton AD, Hall JE. *Textbook of Medical Physiology* (11th ed.). Oxford, UK: Elsevier Health Sciences, 2005.
- Harrison SM, Bers DM. Temperature dependence of myofilament Ca sensitivity of rat, guinea pig, and frog ventricular muscle. *Am J Physiol Cell Physiol* 258: C274–C281, 1990.
- Herrmann C, Houadjeto M, Travers F, Barman T. Early steps of the Mg^{2+} -ATPase of relaxed myofibrils. A comparison with Ca^{2+} -activated myofibrils and myosin subfragment 1. *Biochemistry* 31: 8036–8042, 1992.
- Hodgkin AL, Huxley AF. A quantitative description of membrane current and its application to conduction and excitation in nerve. *J Physiol* 117: 500–544, 1952.
- Hren R. *A Realistic Model of the Human Ventricular Myocardium: Application of the Study of Actopic Activation* (PhD thesis). Halifax, NS, Canada: Dalhousie Univ., 1996.
- Hren R, Nenonen J, Horacek BM. Simulated epicardial potential maps during paced activation reflect myocardial fibrous structure. *Ann Biomed Eng* 26: 1022–1035, 1998.
- Hu H, Sachs F. Stretch-activated ion channels in the heart. *J Mol Cell Cardiol* 29: 1511–1523, 1997.
- Huang J, Rogers JM, Killingsworth CR, Singh KP, Smith WM, Ideker R. Evolution of activation patterns during long-duration ventricular fibrillation in dogs. *Am J Physiol Heart Circ Physiol* 286: H1139–H1200, 2004.
- Hunter PJ, McCulloch AD, ter Keurs HE. Modelling the mechanical properties of cardiac muscle. *Prog Biophys Mol Biol* 69: 289–331, 1998.
- Hunter PJ, Nash MP, Sands GB. Computational electromechanics of the heart. In: *Computational Biology of the Heart*, edited by Panfilov AV, Holden AV. Chichester, UK: Wiley, 1997, p. 345–407.
- Janse MJ, Coronel R, Wilms-Schopman FJ, de Groot JR. Mechanical effects on arrhythmogenesis: from pipette to patient. *Prog Biophys Mol Biol* 82: 187–195, 2003.

30. Jie X, Gurev V, Trayanova N. Mechanisms of mechanically induced spontaneous arrhythmias in acute regional ischemia. *Circ Res* 106: 185–192, 2010.
31. Jongsma HJ, Wilders R. Gap junctions in cardiovascular disease. *Circ Res* 86: 1193–1197, 2000.
32. Keener J, Sneyd J. *Mathematical Physiology*. New York: Springer-Verlag, 1998.
33. Keldermann RH, Ten Tusscher KH, Nash MP, Bradley CP, Hren R, Taggart P, Panfilov AV. A computational study of mother rotor VF in the human ventricles. *Am J Physiol Heart Circ Physiol* 296: H370–H379, 2009.
34. Keldermann RH, Nash MP, Panfilov AV. Modeling cardiac mechano-electrical feedback using reaction-diffusion-mechanics systems. *Physica D* 238: 1000–1007, 2009.
35. Kerckhoffs RC, Neal ML, Gu Q, Bassingthwaite JB, Omens JH, McCulloch AD. Coupling of a 3D finite element model of cardiac ventricular mechanics to lumped systems models of the systemic and pulmonary circulation. *Ann Biomed Eng* 35: 1–18, 2007.
36. Kohl P, Day K, Noble D. Cellular mechanisms of cardiac mechano-electric feedback in a mathematical model. *Can J Cardiol* 14: 111–119, 1998.
37. Kohl P, Hunter PJ, Noble D. Stretch-induced changes in heart rate and rhythm: clinical observations, experiments and mathematical models. *Prog Biophys Mol Biol* 71: 91–138, 1999.
38. Kohl P, Ravens U. (editors). *Mechano-Electric Feedback and Cardiac Arrhythmias*. Oxford, UK: Elsevier, 2003, vol. 82, p. 1–266.
39. Malvern LE. *Introduction to the Mechanics of a Continuous Medium*. Englewood Cliffs, NJ: Prentice Hall, 1969.
40. McCulloch AD, Smaill BH, Hunter PJ. Left ventricular epicardial deformation in the isolated arrested dog heart. *Am J Physiol Heart Circ Physiol* 252: H233–H241, 1987.
41. Moreno J, Zaitsev AV, Warren M, Berenfeld O, Kalifa J, Lucca E, Mironov S, Guha P, Jalife J. Effect of remodeling, stretch and ischaemia on ventricular fibrillation frequency and dynamics in a heart failure model. *Cardiovasc Res* 65: 158–166, 2005.
42. Morgan JM, Cunningham D, Rowland E. Dispersion of monophasic action potential duration: demonstrable in humans after premature ventricular extrastimulation but not in steady state. *J Am Coll Cardiol* 19: 1244–1253, 1992.
43. Nanthakumar K, Walcott GP, Melnick S, Rogers JM, Kay MW, Smith WM, Ideker RE, Holman W. Epicardial organization of human ventricular fibrillation. *Heart Rhythm* 1: 14–23, 2004.
44. Nash MP, Bradley CP, Sutton PM, Clayton RH, Kallis P, Hayward MP, Paterson DJ, Taggart P. Whole heart action potential duration restitution properties in cardiac patients: a combined clinical and modeling study. *Exp Physiol* 91: 339–354, 2006.
45. Nash MP, Hunter PJ. Computational mechanics of the heart: from tissue structure to ventricular function. *J Elasticity* 61: 113–141, 2000.
46. Nash MP, Mourad A, Clayton RH, Sutton PM, Bradley CP, Hayward M, Paterson DJ, Taggart P. Evidence for multiple mechanisms in human ventricular fibrillation. *Circulation* 114: 536–542, 2006.
47. Nash MP, Panfilov AV. Electromechanical model of excitable tissue to study reentrant cardiac arrhythmias. *Prog Biophys Mol Biol* 85: 501–522, 2004.
48. Niederer SA, Hunter PJ, Smith NP. A quantitative analysis of cardiac myocyte relaxation: a simulation study. *Biophys J* 90: 1697–1722, 2006.
49. Niederer SA, Smith NP. An improved numerical method for strong coupling of excitation and contraction models in the heart. *Prog Biophys Mol Biol* 96: 90–111, 2008.
50. Nielsen PM, Le Grice IJ, Smaill BH, Hunter PJ. Mathematical model of geometry and fibrous structure of the heart. *Am J Physiol Heart Circ Physiol* 260: H1365–H1378, 1991.
51. Omens JH, MacKenna DA, McCulloch AD. Measurement of strain and analysis of stress in resting rat left ventricular myocardium. *J Biomech* 26: 665–676, 1993.
52. Panfilov AV, Keldermann RH, Nash MP. Self-organized pacemakers in a coupled reaction-diffusion-mechanics system. *Phys Rev Lett* 95: 258104, 2005.
53. Panfilov AV, Keldermann RH, Nash MP. Drift and breakup of spiral waves in reaction-diffusion-mechanics systems. *Proc Natl Acad Sci USA* 104: 7922–7926, 2007.
54. Panfilov AV, Pertsov AM. Ventricular fibrillation: evolution of the multiple wavelet hypothesis. *Philos Trans R Soc Lond A Math Phys Sci* 359: 1315–1325, 2001.
55. Parmley WW, Sonnenblick EH. Relation between mechanics of contraction and relaxation in mammalian cardiac muscle. *Am J Physiol* 216: 1084–1091, 1969.
56. Piroddi N, Belus A, Scellini B, Tesi C, Giunti G, Cerbai E, Mugelli A, Poggesi C. Tension generation and relaxation in single myofibrils from human atrial and ventricular myocardium. *Pflügers Arch* 454: 63–73, 2007.
57. Plonsey R, Barr RC. *Bioelectricity*. New York: Plenum, 1989.
58. Rodriguez EK, Hunter WC, Royce MJ, Leppo MK, Douglas AS, Weisman HF. A method to reconstruct myocardial sarcomere lengths and orientations at transmural sites in beating canine hearts. *Am J Physiol Heart Circ Physiol* 263: H293–H306, 1992.
59. Sigurdson W, Ruknudin A, Sachs F. Calcium imaging of mechanically induced fluxes in tissue-cultured chick heart: role of stretch-activated ion channels. *Am J Physiol Heart Circ Physiol* 262: H1110–H1115, 1992.
60. Streeter DD Jr. Gross morphology of the heart. In: *Handbook of Physiology. The Cardiovascular System. The Heart*. Bethesda, MD: Am. Physiol. Soc., 1979, sect. 2, Vol. I, chapt. 4, p. 61–112.
61. Taggart P, Sutton PM, Opthof T, Coronel R, Trimlett R, Pugsley W, Kallis P. Inhomogeneous transmural conduction during early ischaemia in patients with coronary artery disease. *J Mol Cell Cardiol* 32: 621–630, 2000.
62. Ten Tusscher KH, Mourad A, Nash MP, Clayton RH, Bradley CP, Paterson DJ, Hren R, Hayward M, Panfilov AV, Taggart P. Organization of ventricular fibrillation in the human heart: experiments and models. *Exp Physiol* 94: 553–562, 2009.
63. Ten Tusscher KH, Hren R, Panfilov AV. Organization of ventricular fibrillation in the human heart. *Circ Res* 100: e87–e101, 2007.
64. Ten Tusscher KH, Panfilov AV. Alternans and spiral breakup in a human ventricular tissue model. *Am J Physiol Heart Circ Physiol* 291: H1088–H1100, 2006.
65. Ter Keurs HE, Rijnsburger WH, Van Heuningen R, Nagelsmit MJ. Tension development and sarcomere length in rat cardiac trabeculae. Evidence of length-dependent activation. *Circ Res* 46: 703–714, 1980.
66. Ter Keurs HE, Shinozaki T, Zhang YM, Zhang ML, Wakayama Y, Sugai Y, Kagaya Y, Miura M, Boyden PA, Stuyvers BD, Landesberg A. Sarcomere mechanics in uniform and non-uniform cardiac muscle: A link between pump function and arrhythmias. *Prog Biophys Mol Biol* 97: 312–331, 2008.
67. Trayanova N, Li W, Eason J, Kohl P. Effect of stretch activated channels on defibrillation efficacy. *Heart Rhythm* 1: 67–77, 2004.
68. Valderrabano M, Chen P, Lin SF. Spatial distribution of phase singularities in ventricular fibrillation. *Circulation* 108: 354–359, 2003.
69. Vetter FJ, McCulloch AD. Mechano-electric feedback in a model of the passively inflated left ventricle. *Ann Biomed Eng* 29: 414–426, 2001.
70. Witkowski FX, Leon LJ, Penkoske PA, Giles WR, Spano ML, Ditto EL, Winfree AT. Spatiotemporal evolution of ventricular fibrillation. *Nature* 392: 78–82, 1998.
71. Wu TJ, Ong JJ, Hwang C, Lee JJ, Fishbein MC, Czer L, Tento A, Blanche C, Kass RM, Mandel WJ, Karagueuzian HS, Chen P. Characteristics of wave fronts during ventricular fibrillation in human hearts with dilated cardiomyopathy: role of increased fibrosis on the generation of reentry. *J Am Coll Cardiol* 32: 187–196, 1998.
72. Zeng T, Bett GC, Sachs F. Stretch-activated whole cell currents in adult rat cardiac myocytes. *Am J Physiol Heart Circ Physiol* 278: H548–H557, 2000.
73. Zevitz ME. WebMD. eMedicine. Ventricular Fibrillation (online). <http://emedicine.medscape.com/article/158712-overview> (5 May 2010).
74. Zhang H, Holden AV, Kodama I, Honjo H, Lei M, Varghese T, Boyett MR. Mathematical models of action potentials in the periphery and center of the rabbit sinoatrial node. *Am J Physiol Heart Circ Physiol* 279: H397–H421, 2000.
75. Zhang YH, Hancox JC. Gadolinium inhibits Na⁺-Ca²⁺ exchanger current in guinea-pig isolated ventricular myocytes. *Br J Pharmacol* 130: 485–488, 2000.